3-D subsurface displacement and strain fields for faults and fault arrays in a layered elastic half-space

X. Q. Ma and N. J. Kusznir
Department of Earth Sciences, University of Liverpool, PO Box 147, Liverpool L69 3BX, UK

SUMMARY
A quantitative model using elastic dislocation theory has been developed to model the near-field subsurface displacement field associated with faults and fault arrays within an elastic layer above an elastic half-space. A fault is modelled as a surface across which there is a discontinuity in prescribed displacements. Fault displacements may be oblique as well as dip–slip. The mathematical expressions for the surface and subsurface displacements are formed using the Thomson–Haskell matrix technique. Faults may intersect the free surface or may be blind. The model has been used to determine the 3-D surface and subsurface displacement fields for a rectangular fault with constant slip and for an elliptical fault on which the slip varies from a point of maximum displacement at the centre to zero displacement at an elliptical tip-line. The 3-D displacement field and associated strain tensor may be determined for individual slip events on a fault or for cumulative fault displacements. Displacement contour maps may be constructed for either originally horizontal, vertical or inclined horizons. The model has also been applied to multiple fault arrays.

Key words: coseismic subsurface fault displacement, elastic dislocation.

1 INTRODUCTION

A fault may be regarded as a dislocation created by fracture of the rock material separating two rock masses. During fracture the two opposing fault surfaces suffer displacement with respect to each other. The static coseismic deformation associated with earthquake faults has been studied extensively using elastic dislocation theory. Many methods based on the elastic dislocation theory are available to calculate surface displacements in a homogeneous half-space (Chinnery 1961; Maruyama 1964; Savage & Hastie 1966; Mansinha & Smylie 1971) and in a layered half-space (Ben-Menahem & Gillon 1970; Jovanovich, Husseini & Chinnery 1974a; Rundle 1982).

The main aims of previous studies have been to interpret geodetic observations and to derive earthquake source parameters such as rupture zone size, depth of hypocentre, seismic moment and stress drop (Savage & Hastie 1966; Mikumo 1973). Traditionally, the elastic dislocation theory has been used to compute surface displacement only. Recently Roth (1990) derived new kernel functions for subsurface displacements associated with point sources within a layered elastic medium. However, Roth's determination of displacement fields was restricted to an area below the free surface and above the point source level. In studying the deformation generated by a finite size fault, most workers assumed that the fault surface is a rectangular plane with constant slip. Real faults do not possess a rectangular geometry neither do they have constant displacements.

The objective of the work described in this paper is to determine 3-D subsurface displacement and strain fields for a fault with a more realistic fault geometry and displacement distribution. The well-developed Thomson–Haskell Matrix technique has been used to derive new kernel functions for displacement below a point source. The theory developed by Jovanovich *et al.* (1974a) and Roth (1990) has been extended further to compute the displacement field at any point surrounding a fault in the upper elastic layer. A new formulation has been derived which permits displacements to be determined at the free surface, or in the subsurface either above or below the source. For the purpose of comparison and testing against existing theory, the developed model has been used to compute the 3-D surface displacement field for a rectangular fault with constant slip for which existing solutions are available.

The subsurface displacement fields for such a simple rectangular fault are also shown. Surface and subsurface

displacement fields have also been determined for a more realistic fault geometry and displacement distribution in which the slip varies from a point of maximum displacement at the centre to zero displacement at an elliptical tip-line as suggested by the fault growth model proposed by Walsh & Watterson (1987). The control by fault dip, fault depth and fault slip direction on subsurface displacement fields has been explored. The developed mathematical model has also been used to determine the strain fields (normal and volumetric strains) associated with single faults. As well as being applied to the cumulative fault displacement field, the new model has also been used to determine the incremental subsurface displacement field associated with a single fault slip event, corresponding to a single seismic cycle.

2 THEORY

In the following work the modelling of displacements due to earthquake faulting using elastic dislocation theory will be restricted to dealing with the static problem only. Waves and transient dynamic features associated with the earthquake will be neglected. It is also assumed that the effects of the Earth's curvature, its gravity and temperature on the displacement field are negligible. The elastic continuum will also be assumed to be isotropic so that the laws of classical linear elasticity apply.

The use of dislocation theory to determine the static deformation accompanying faulting within a semi-infinite, isotropic, elastic medium has been discussed by Steketee (1958a, b) who developed a Green's function method to calculate the stresses and displacements produced by a strike–slip fault. Maruyama (1964) derived the remaining five sets of Green's functions, which allow the displacement field due to an arbitrary displacement dislocation in a semi-infinite medium to be determined through the Volterra relation. Rybicki (1971) presented analytical solutions for a 2-D strike–slip fault both in an infinite homogeneous half-space and a layered half-space. Sato (1971) developed a method of calculating surface displacements for 3-D strike–slip and dip–slip faults in a layered elastic medium. The practical applications of elastic dislocation theory to rectangular earthquake faults in an elastic half-space were addressed by Chinnery (1961), Savage & Hastie (1966) and Mansinha & Smylie (1971). Ben-Menahem & Singh (1968) extended the results of Steketee and Maruyama to a layered half-space. Singh (1970) applied the Thomson–Haskell propagation matrix technique to solve the problem of the static deformation of a multilayered elastic half-space. Each layer of the multilayered medium is assumed to be homogeneous and isotropic, and interfaces are assumed to be in welded contact. The point source is represented as a discontinuity in the depth-dependent coefficients of the displacement and stress at the source level. Following Singh, Jovanovich et al. (1974a) described a procedure for the numerical evaluation of the kernel functions.

In this paper, we deal with a model consisting of one elastic layer overlying an elastic half-space. It is obvious that the results can easily be extended to a multilayer model by introducing extra layer matrices. The integral expressions used for calculating displacements are from Singh (1970) and Javanovich et al. (1974a). The expressions of the kernel functions for subsurface displacements above a source level

are from Roth (1990). In this paper, we derive the new kernel functions for subsurface displacements below a source level. Those who are particularly interested in the mathematical background and derivations should refer to the cited papers.

Fig. 1(a) shows a cylindrical coordinate system (r, φ, z) with the z-axis positive downwards. A point source representing an infinitesimal dislocated fault surface is located at $(r = 0, z = h)$. β is the rake of the fault, and γ is the dip of the fault. The strike of the point source is taken along the x-axis while the slip is taken with respect to the hanging wall. Fig. 1(b) shows an elastic layer of thickness H overlying an elastic half-space for which we will determine the generalized 3-D fault displacement field. The point source is located at $z = h$ within the top layer. The
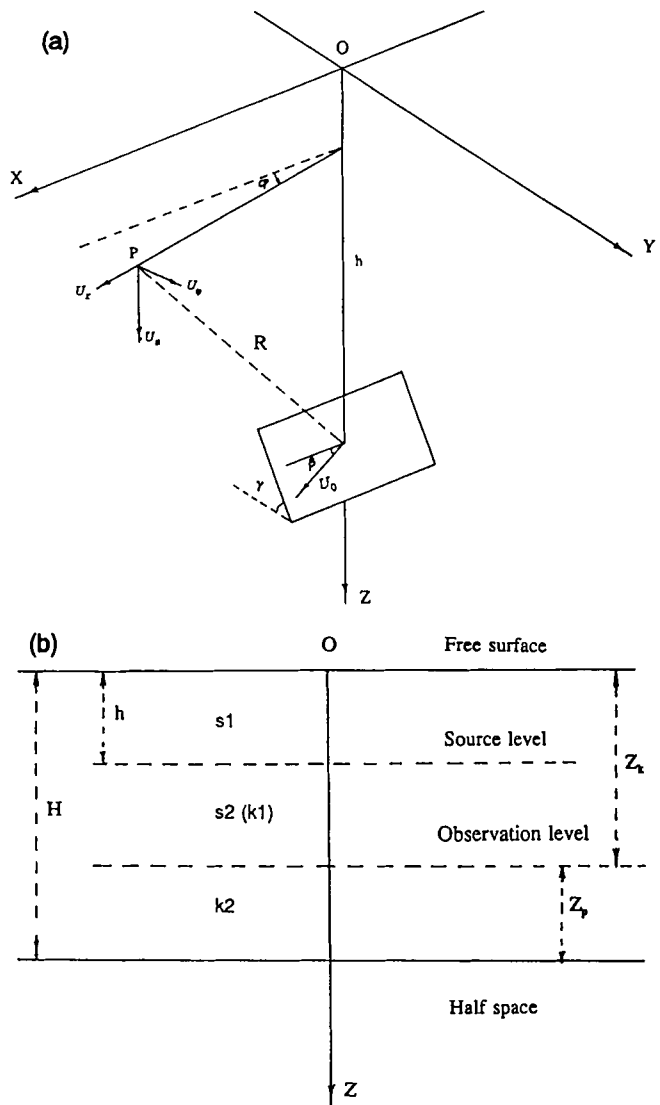
Figure 1. (a) Geometry of arbitrary fault in the cylindrical coordinate system (r, φ, z) with origin O. P is the point of observation at a distance R from the source. β, γ and U_0 are the rake, dip and slip respectively. The strike is taken along the x-axis. (b) Model used for computations—an elastic layer $(H = 35\,\text{km})$ above an elastic half-space. The source level is at depth h. Lame's constants are: $\mu_1 = 7.0 \times 10^{10}\,\text{N m}^{-2}$, $\lambda_1 = 8.22 \times 10^{10}\,\text{N m}^{-2}$; $\mu_2 = 1.55 \times 10^{11}\,\text{N m}^{-2}$, $\lambda_2 = 1.82 \times 10^{11}\,\text{N m}^{-2}$.

observation points may be either on the free surface or on an horizon $z = z_k$ which can be above or below the source level. Numerical values of elastic constants are listed in the caption of Fig. 1. This two-layer model will be used throughout this paper.

The vector displacement $\mathbf{u}_n$, in the nth layer, satisfies the Navier equation of static elasticity for an infinite medium.

$$[\nabla^2 + (1 + \lambda_n/\mu_n) \, \text{grad div}]\mathbf{u}_n = 0. \tag{1}$$

Three independent vector solutions of equation (1) for $\mathbf{u}_n$ are given by

$$\mathbf{N}^{\pm}_{nm} = \exp(\pm kz)(\pm \mathbf{P}_m + \mathbf{B}_m),$$

$$\mathbf{F}^{\pm}_{nm} = \exp(\pm kz)[(\pm 1 - 2\delta_n kz)\mathbf{P}_m - (1 + 2\delta_n kz)\mathbf{B}_m], \tag{2}$$

$$\mathbf{M}^{\pm}_{nm} = \exp(\pm kz)\mathbf{C}_m,$$

where $\delta_n = (\lambda_n + \mu_n)/(\lambda_n + 3\mu_n)$ and $\mathbf{P}_m, \mathbf{B}_m$ and $\mathbf{C}_m$ are three cylindrical basis vectors.

$$\mathbf{P}_m = \mathbf{e}_z J_m(kr) \exp(im\varphi),$$

$$\mathbf{B}_m = \left(\mathbf{e}_r \frac{\partial}{\partial kr} + \mathbf{e}_\varphi \frac{1}{kr}\frac{\partial}{\partial \varphi}\right) J_m(kr) \exp(im\varphi), \tag{3}$$

$$\mathbf{C}_m = \left(\mathbf{e}_r \frac{1}{kr}\frac{\partial}{\partial \varphi} - \mathbf{e}_\varphi \frac{\partial}{\partial kr}\right) J_m(kr) \exp(im\varphi),$$

where $\mathbf{e}_z, \mathbf{e}_\varphi, \mathbf{e}_r$ are the orthogonal triad of unit vectors in the z, φ and r directions respectively.

The general solution of equation (1) is expressed in the spatial domain as a sum of integrals in the wavenumber domain.

$$\mathbf{u}_n = \sum_m \int_0^\infty \mathbf{u}_{nm}(k)k \, dk, \tag{4}$$

where $\mathbf{u}_{nm}$ is a linear combination of the three independent vector solutions

$$\mathbf{u}_{nm}(k) = A'_{nm}\mathbf{N}^-_{nm} + A''_{nm}\mathbf{N}^+_{nm} + B'_{nm}\mathbf{F}^-_{nm} + B''_{nm}\mathbf{F}^+_{nm}$$

$$+ C'_{nm}\mathbf{M}^-_{nm} + C''_{nm}\mathbf{M}^+_{nm}, \tag{5}$$

where A'_{nm}, A''_{nm}, B'_{nm}, B''_{nm} are layer coefficients.

By substituting (2) into (5), we get:

$$\mathbf{u}_{nm}(k) = x_{nm}\mathbf{P}_m + y_{nm}\mathbf{B}_m + z_{nm}\mathbf{C}_m, \tag{6}$$

where x_{nm}, y_{nm} and z_{nm} are kernel functions in which subscript n denotes layer number and subscript m depends on source slip vector.

$$x_{nm} = -\exp(-kz)A'_{nm} + \exp(kz)A''_{nm} - (1 + 2\delta_n kz)$$

$$\times \exp(-kz)B'_{nm} + (1 - 2\delta_n kz)\exp(kz)B''_{nm},$$

$$y_{nm} = \exp(-kz)A'_{nm} + \exp(kz)A''_{nm} - (1 - 2\delta_n kz) \tag{7}$$

$$\times \exp(-kz)B'_{nm} - (1 + 2\delta_n kz)\exp(kz)B''_{nm},$$

$$z_{nm} = \exp(-kz)C'_{nm} + \exp(kz)C''_{nm}.$$

The stress vector $\mathbf{T}_{nm}$ across a plane of constant z associated with the displacement $\mathbf{u}_{nm}$ is given by

$$\mathbf{T}_{nm} = 2kX_{nm}\mathbf{P}_m + 2kY_{nm}\mathbf{B}_m + kZ_{nm}\mathbf{C}_m, \tag{8}$$

where X_{nm}, Y_{nm} and Z_{nm} are kernel functions for stress vectors, which can be expressed in a similar form (7).

In order to determine the kernel functions, Singh (1970) split the problem into 'R' and 'L' problems. He applied the

conditions of zero normal traction for the free surface at $z = 0$, those of zero displacement, stress and potential at infinite depth, and displacement and stress continuity across layer boundaries. He incorporated a source by creating a layer boundary at the source depth h and prescribing appropriate discontinuity conditions across the boundary for the source. By further using the Haskell matrix relationship, he derived the kernel function expressions for calculating surface displacements.

$$x_{1m}(0) = [(E_{11}E_{43} - E_{13}E_{41})(F_m)_3 + (E_{13}E_{31} - E_{11}E_{33})$$

$$\times (F_m)_4]/[E_{31}E_{43} - E_{33}E_{41}) - (F_m)_1],$$

$$y_{1m}(0) = [(E_{21}E_{43} - E_{23}E_{41})(F_m)_3 + (E_{23}E_{31} - E_{21}E_{33}) \tag{9}$$

$$\times (F_m)_4]/[(E_{31}E_{43} - E_{33}E_{41}) - (F_m)_2],$$

$$z_{1m}(0) = [E^L_{11}(F_m)^L_2 - E^L_{21}(F^L_m)_1]/E^L_{21}.$$

The **(E)** matrices and the **(F$_m$)** vectors for a single layer overlying a half-space are given by:

$$\mathbf{E} = \mathbf{a}_1[Z_p(H)],$$

$$\mathbf{E}^L = \mathbf{a}^L_1[Z_p(H)^L],$$

$$\mathbf{F}_m = \mathbf{a}_{s1}\mathbf{D}_m, \tag{10}$$

$$\mathbf{F}^L_m = \mathbf{a}^L_{s1}\mathbf{D}^L_m,$$

where $\mathbf{a}_1$ and $\mathbf{a}^L_1$ are the layer matrices, $[Z_p(H)]$ and $[Z^L_p(H)]$ are the coefficient matrices of the half-space, and $\mathbf{D}_m$ and $\mathbf{D}^L_m$ are the source vectors, which are determined from the property of the discontinuities in displacement and stress at the source level.

By using a similar technique, Roth (1990) derived the kernel functions for subsurface displacements above the source level. The kernel functions derived by Roth are:

$$x_{km}(z_k) = \{E^*_{11}[E_{43}(F_m)_3 - E_{33}(F_m)_4] + E^*_{13}[E_{31}(F_m)_4$$

$$- E_{41}(F_m)_3]\}/[(E_{31}E_{43} - E_{33}E_{41}) - (F^*_m)_1],$$

$$y_{km}(z_k) = \{E^*_{21}[E_{43}(F_m)_3 - E_{33}(F_m)_4] + E^*_{23}[E_{31}(F_m)_4 \tag{11}$$

$$- E_{41}(F_m)_3]\}/[(E_{31}E_{43} - E_{33}E_{41}) - (F^*_m)_2],$$

$$z_{km}(z_k) = [E^{*L}_{11}(F^L_m)_2 - E^L_{21}(F^{*L}_m)_1]/E^L_{21},$$

and

$$\mathbf{E}^* = (a_{k2p})[Z_p(H)],$$

$$\mathbf{E}^{*L} = (a^L_{k2p})[Z_p(H)^L],$$

$$\mathbf{F}^*_m = (a_{k2s})\mathbf{D}_m, \tag{12}$$

$$\mathbf{F}^{*L}_m = (a^L_{k2s})\mathbf{D}^L_m,$$

where (a_{k2p}) and (a^L_{k2p}) are matrices for the layer bounded by the observation horizon and the top boundary of the half-space, while (a_{k2s}) and (a^L_{k2s}) are the matrices for the layer bounded by the observation horizon and the source horizon.

Roth did not however derive the kernel functions for displacement beneath the source. To determine the kernel functions for the displacements below the source level, we divide the top layer into three layers, $s1$, $s2$ and $k2$ (Fig. 1b). The lower boundary of the first layer ($s1$) corresponds to the source level, where there are discontinuities in stresses and displacements. The lower boundary of the second layer ($s2$) is an horizon where observations are made. As shown in Fig. 1(b), the source is at $z = h$, and the

observation points are at z_k. If we let n in equation (22) of Singh (1970) be $k2$, we get:

$$A_{k2m}(z_{s2}) = a_{k2}A_{k2m}(z_{k2}).$$ (13)

Using (18) and (19) and boundary conditions in Singh, we get:

$$x_{k2m}(z_{s2}) = E_{11}^\pounds A_{pm}' + E_{13}^\pounds B_{pm}',$$
$$y_{k2m}(z_{s2}) = E_{21}^\pounds A_{pm}' + E_{23}^\pounds B_{pm}',$$ (14)

where

$$\mathbf{E}^\pounds = a_{k2}[Z_p(H)].$$

A_{pm}' and B_{pm}' are coefficients for the half space and taken as those determined for surface displacements.

By arranging (14), we get:

$$x_{k2m}(z_{s2}) = \{E_{11}^\pounds[E_{43}(F_m)_3 - E_{33}(F_m)_4] + E_{13}^\pounds[E_{31}(F_m)_4$$
$$- E_{41}(F_m)_3]\}/(E_{31}E_{43} - E_{33}E_{41}),$$
$$y_{k2m}(z_{s2}) = \{E_{21}^\pounds[E_{43}(F_m)_3 - E_{33}(F_m)_4] + E_{23}^\pounds[E_{31}(F_m)_4$$
$$- E_{41}(F_m)_3]\}/(E_{31}E_{43} - E_{33}E_{41}).$$ (15)

The solution of the 'L' problem can be solved in the similar way, it is:

$$z_{k2m}^L(z_{s2}) = E_{11}^{\pounds L}[(F_m^L)_2/E_{21}^L],$$ (16)

where

$$\mathbf{E}^{\pounds L} = a_{k2}^L[Z_p^L(H)].$$

The above solutions can easily be extended to those for a multilayered medium.

Jovanovich *et al.* (1974a) derived the integral expressions for surface displacements for a vertical strike–slip, a vertical dip–slip and a 45° dip–slip point source. These expressions can also be used for subsurface displacements if the kernel functions for the surface displacements are replaced by those for subsurface displacements [see (17)–(19)].

(i) For a vertical strike–slip source,

$$\mathbf{u}_r = -\int_0^\infty [(1/i)y_{12}(z_{s2})(\partial/\partial kr)J_2(kr)$$
$$+ z_{12}(z_{s2})(2/kr)J_2(kr)]k\,dk\,\sin 2\varphi,$$

$$\mathbf{u}_\varphi = -\int_0^\infty [(1/i)y_{12}(z_{s2})(2/kr)J_2(kr)$$ (17)
$$+ z_{12}(z_{s2})(\partial/\partial kr)J_2(kr)]k\,dk\,\cos 2\varphi,$$

$$\mathbf{u}_z = -\int_0^\infty [(1/i)x_{12}(z_{s2})J_2(kr)]k\,dk\,\sin 2\varphi.$$

(ii) For a vertical dip–slip source,

$$\mathbf{u}_r = -\int_0^\infty [(1/i)y_{11}(z_{s2})(\partial/\partial kr)J_1(kr)$$
$$+ z_{11}(z_{s2})(1/kr)J_1(kr)]k\,dk\,\sin\varphi,$$

$$\mathbf{u}_\varphi = -\int_0^\infty [(1/i)y_{11}(z_{s2})[1/kr)J_1(kr)$$ (18)
$$+ z_{11}(z_{s2})(\partial/\partial kr)J_1(kr)]k\,dk\,\cos\varphi,$$

$$\mathbf{u}_z = -\int_0^\infty [(1/i)x_{11}(z_{s2})J_1(kr)]k\,dk\,\sin\varphi.$$

(iii) For a 45° dip–slip source,

$$\mathbf{u}_r = -\int_0^\infty \{y_{10}(z_{s2})J_1(kr) + [(1/i)z_{12}(z_{s2})(2/kr)J_2(kr)$$
$$- y_{12}(z_{s2})(\partial/\partial kr)J_2(kr)]\cos 2\varphi\}k\,dk,$$

$$\mathbf{u}_\varphi = -\int_0^\infty [(2/kr)y_{12}(z_{s2})J_2(kr) - (1/i)z_{12}(z_{s2})$$ (19)
$$\times (\partial/\partial kr)J_2(kr)]k\,dk\,\sin 2\varphi,$$

$$\mathbf{u}_z = \int_0^\infty [x_{10}(z_{s2})J_0(kr) + x_{12}(z_{s2})J_2(kr)\cos 2\varphi]k\,dk,$$

where x_{nm}, y_{nm}, z_{nm} are kernel functions, and J_m are Bessel functions.

The displacement field due to an arbitrary point source located at $(r = 0, z = h)$ can be expressed in terms of three basic point source responses. The displacement components are:

$$\mathbf{u}_i = \sin\beta\,(u_i^3\sin 2\gamma - u_i^2\cos 2\gamma)$$
$$+ \cos\beta\,(u_i^1\sin\gamma - u_i^4\cos\gamma),$$ (20)

where β and γ specify the orientation of the source, as shown in Fig. 1(a). The displacement u_i^1, u_i^2, u_i^3 are respectively the solutions for a vertical strike–slip source, a vertical dip–slip source and a 45° dip–slip source. The equation for u_i^4 is the same as that for u_i^2 with φ replaced by $(\varphi - \pi/2)$ (Jovanovich *et al.* 1974a).

3 NUMERICAL EVALUATION

While it might appear that the evaluation of equations (17)–(19) to determine 3-D subsurface displacement field is a straight forward process, this is unfortunately not so. Since the kernel functions involve matrix products of highly disproportionate magnitudes dependent on the product of layer thickness H and wavenumber k, some numerical problems arise due to the fact that one must add hyperbolic sines and cosines of argument kH which introduces round-off errors as kH increases. In order to avoid numerical overflow and underflow, the upper limit of wavenumber k in the integration has to be limited. As a result, the high-frequency components in displacements are lost especially within the near field, and the calculated displacements are not stable. In order to overcome this problem, we use a similar numerical method as proposed by Jovanovich *et al.* (1974a), to decompose the matrix a_n and matrix Z_p into the sum of four matrices. The $\mathbf{E}$ matrix may then be written as the product of matrices consisting of constants while all the exponentials and powers of k are carried outside the appropriate matrix product. The numerators of the kernel functions are formed from the second-order subdeterminants of the $\mathbf{E}$ matrix multiplied by the appropriate $\mathbf{F}_m$ terms. The denominators, which are only the second-order subdeterminant of the $\mathbf{E}$ matrix, are treated in the same way as proposed by Ben-Menahem & Gillon (1970), i.e. the denominator is approximated by a truncated binomial series expansion and then the remainder of the series is fitted with a sum of exponential–polynomial terms using the method of least squares. As the denominator is a function of model parameters such as

physical dimension and elastic properties (λ, μ), the least-square fitting process has to be carried out for each physical model. For a two-layer model, as we have described, the denominator has a relatively simple form (four terms) and the time for computing the non-linear fit is very short. However as the number of layers increases, the expression of the denominator, i.e. the second-order subdeterminant of the **E** matrix, becomes far more complicated and as a consequence the computation time for determining the denominator as well as for the non-linear fit increases. The kernel functions are obtained by multiplying the exact numerator series by the approximated inverse denominator series. For a simple model consisting of one layer overlying a half-space, there are 58 exponential-polynomial terms in the kernel functions of the 'R' problem, and 10 terms for the 'L' problem. The final expressions of surface displacements are the sum of the Lipshitz–Hankell integrals (21), and their exact quadrature can be found in Erdelyi (1954). However, care must be taken in evaluating the associated Legendre polynomials, as individual authors have defined the polynomials in different forms giving a difference of a constant $(-1)^m$.

$$u(r) = \sum_l \sum_n a_{ln} \int_0^\infty k^n e^{(-kD_l)} J_m(kr) \, dk \qquad (21)$$

(where a_{ln} are constant coefficients, and D_l are the exponential arguments which are a function of layer thickness, source depth and depth of an observation point).

In the case of subsurface displacements, the kernel functions have a more complicated form than those for surface displacements because $E_{ik}^* E_{jl} - E_{il}^* E_{jk}$ is no longer simply a second-order subdeterminant of matrix **E**. Although they can be treated in the similar way as the above, the number of terms in the kernel functions of the 'R' problem increases to 180, compared to 58 for surface displacements. Moreover, since the kernel functions take different forms for an observation point above and below the source, they have to be evaluated separately.

The computations have been programmed in Fortran-77 using a Sun Sparc Workstation. For the model described in Section 2, the computation of the surface displacement field for an arbitrary point source takes about 5 s, and about 13 s for the subsurface displacement field. The displacements due to a point source of arbitrary orientation have been obtained using formula (20).
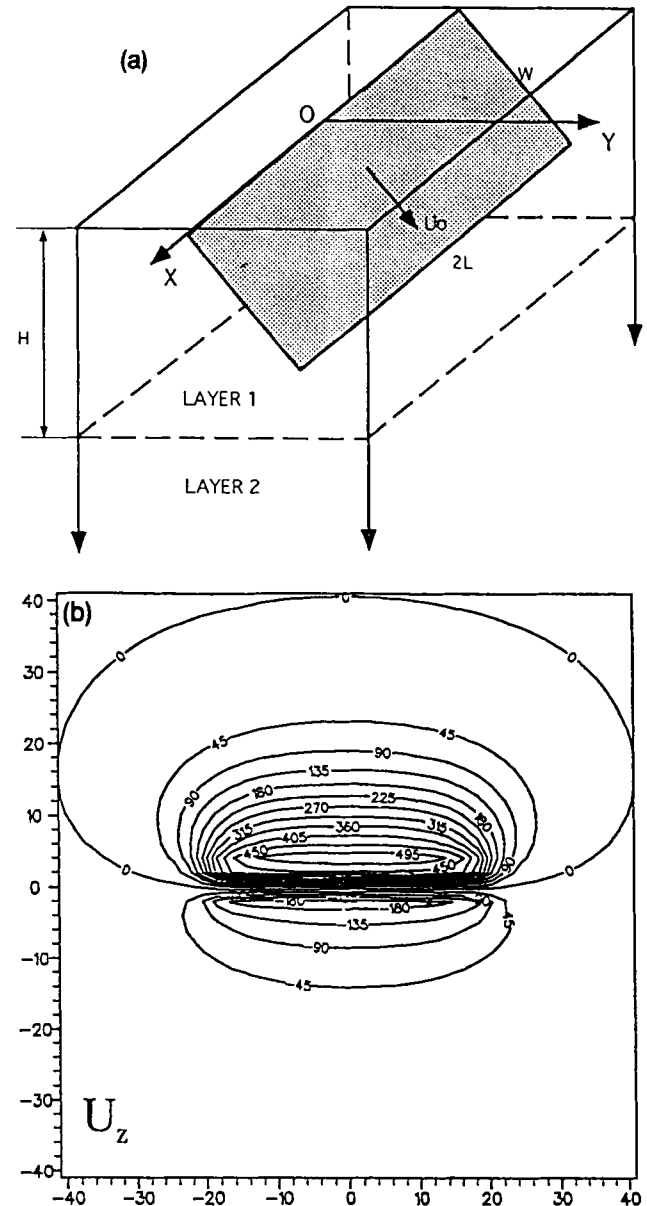
4   RECTANGULAR FAULT WITH CONSTANT SLIP

The surface displacement field for a rectangular dip–slip fault of constant displacement is well known and has been determined by Savage & Hastie (1966) and Rundle (1982). The generalized subsurface displacement model presented in this paper has been used to compute surface displacement for the rectangular constant displacement fault example in order that the newly developed formulation described in this paper may be tested.

Fig. 2(a) shows the coordinate system and geometry for a rectangular dip–slip fault in an elastic layer above an elastic half-space. The fault dips down towards the positive Y direction. The strike of the fault is taken along the X-axis.

In order to determine the displacement field caused by this fault, the fault surface is subdivided by a rectangular grid and the displacement response of a point source is computed at each grid rectangle centre. The displacements due to a dip–slip point source is a linear combination of the response from both a vertical dip–slip and a 45° dip–slip point sources. The total fault displacements are then obtained by integrating the point source responses over the entire fault region.

Consider the example where the length of the fault $(2L)$ is 40 km, the width (W) 20 km, and the constant slip on the

Figure 2. (a) Coordinate system and geometry of a rectangular dip–slip fault of length $2L = 40$ km, width $W = 20$ km, dip $\gamma = 60°$ and constant slip $U_0 = 1$ km. The fault is located within an elastic layer above an elastic half-space and intersects the free surface $(D = 0$ km). (b) Vertical surface displacement (U_z) contour map. Note that positive values correspond to subsidence while negative values correspond to uplift. (c) Horizontal surface displacement (U_x) contour map. (d) Horizontal displacement (U_y) contour map.
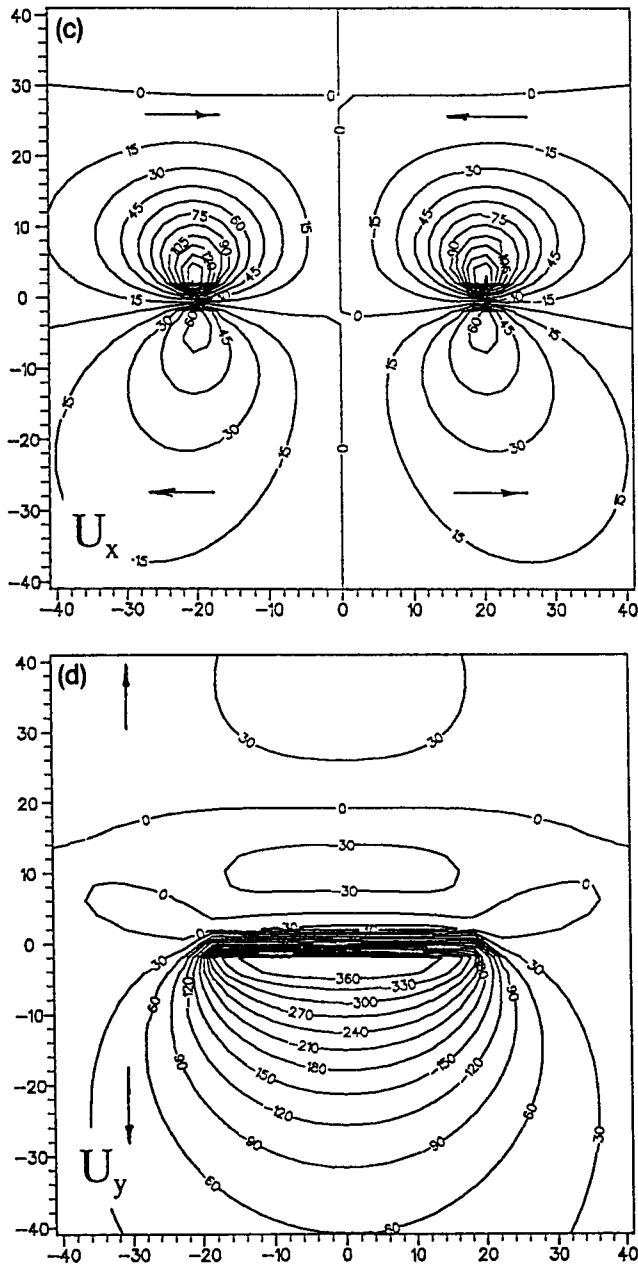
Figure 2. (continued)

conspicuous features in Fig. 2(b) is the asymmetry of the displacement contour pattern, i.e. the uplift marked by negative vertical displacement values are relatively small compared to the subsidence. The degree of this asymmetry varies with fault dips. A vertical fault will show an absolute symmetry in displacements with respect to the fault surface.

When the same model parameters are used as in Rundle's (1982) paper, i.e. $2L = 200$ km, $W = 30$ km, $\gamma = 30°$, the surface deformation calculated by our model is equivalent to the coseismic deformation curve in Rundle's Fig. 2. The comparison of the calculated displacements of a normal fault with those a thrust fault may be made by changing the sign of the displacement.

Subsurface vertical displacements are shown in Fig. 3 for a blind (buried) rectangular fault. The fault dips at 60°, and

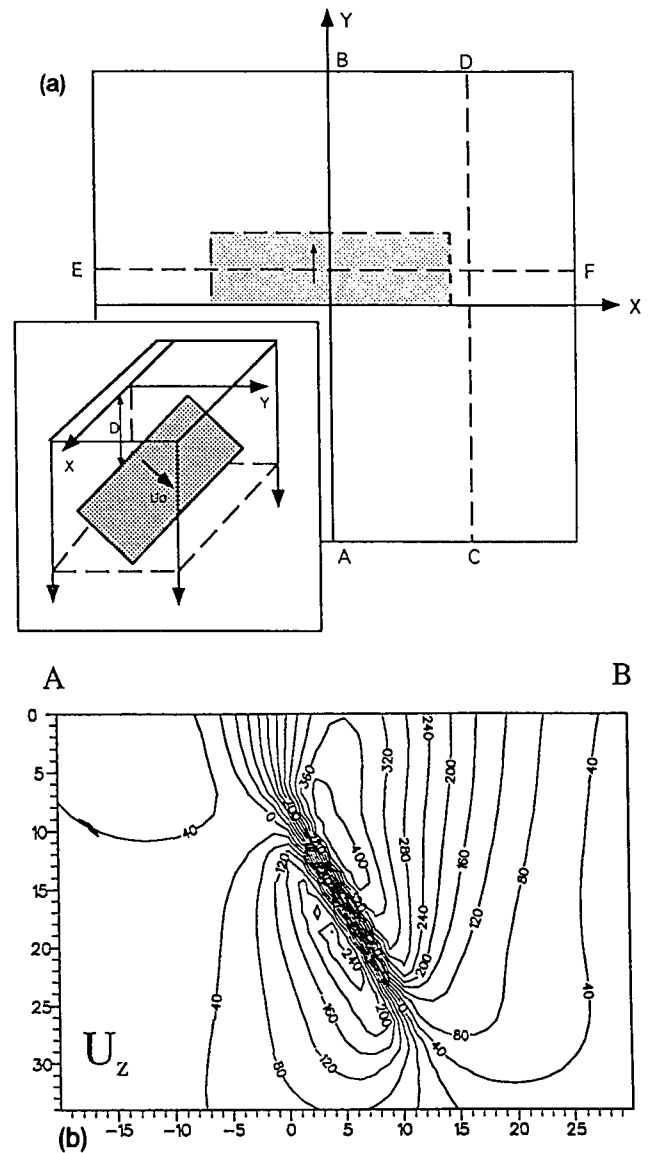fault surface is 1 km. If the grid size is 2 km × 2 km, then the total number of grid elements is 200. Since the kernel functions for a model vary only with the depth and slip of the source, and 20 identical point sources on any rows of the discretized fault surface are at the same depth, and we need to calculate only one point source response on that row. Therefore, for this example only 10 point source responses for 10 different sets of kernel functions need to be computed.

Figs 2(b)–(d) show the surface displacement for a 60° dip–slip fault which cuts through the upper part of the top layer and intercepts the free surface. The arrows on the diagrams indicate the directions of material movement. The material on the downthrow side in Fig. 2(c) moves inwards while on the upthrow side they move outwards. One of the

Figure 3. (a) Plan view of a rectangular fault and three vertical sections. The fault is at depth $D = 8$ km. Both sections AB and EF cut through the fault centre. Section CD is 2 km away from the fault edge. (b) Vertical displacement contour map along the section AB. (c) Vertical displacement contour map along the section CD. (d) Vertical displacement contour map along the section EF.
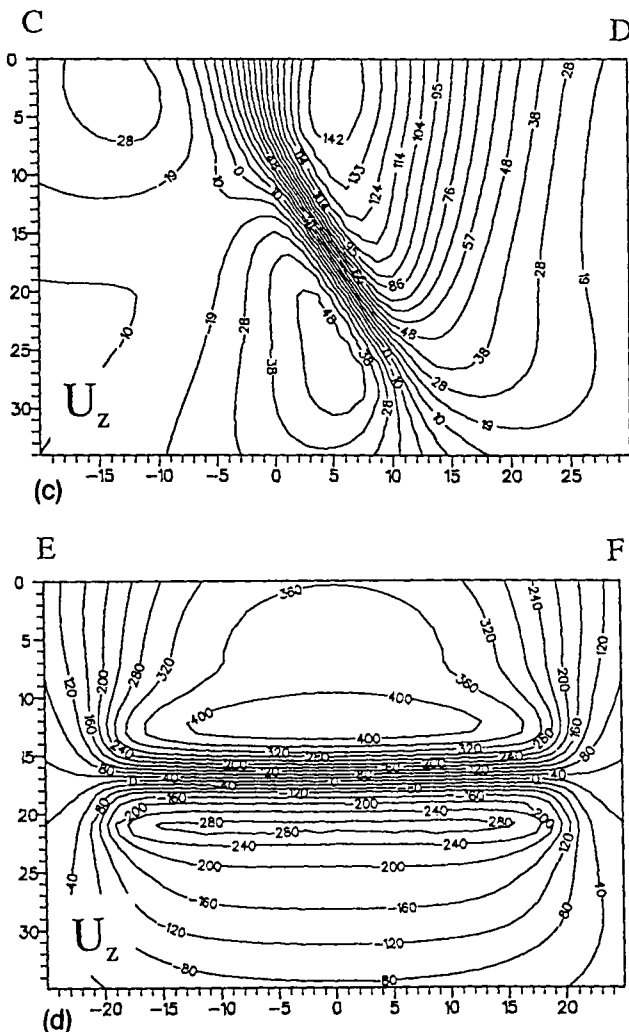
Figure 3. (continued)

is at depth $D = 8$ km from the free surface. The locations of three vertical sections (AB, CD, EF) are shown in Fig. 3(a). Sections AB and CD are normal to the strike of the fault while section EF is parallel to the strike.

Section AB cuts the fault through its centre. Fig. 3(b) is the vertical displacement contour map along section AB, and shows the deformation on both sides of the fault. Positive contour values correspond to subsidence while negative values correspond to uplift. Note that the straight line formed by the zero displacement contour within the fault zone is at an angle of 60° with the horizontal and exactly corresponds to the prescribed dip of the fault. Displacements on each side of the fault are maximum adjacent to the fault and tend to zero downwards and laterally.

Fig. 3(c) shows the vertical displacement contour map on the vertical section CD which is 2 km away from the edge of the fault. In comparison with (b), it can be seen that the displacement values for this section are significantly reduced. Furthermore, the point of maximum displacement on the downthrow side has moved upwards while the point of maximum displacement on the upthrow side of the fault has moved downwards. Although the section does not

intersect the fault surface, a fault zone indicated by closed displacement contours is still apparent. Fig. 3(d) is the displacement contour map on the vertical section EF, and shows two concentric elliptical contour lines within foot and hanging walls. The zero displacement contour line corresponds to the level of the fault centre, which is at 16.6 km depth below.
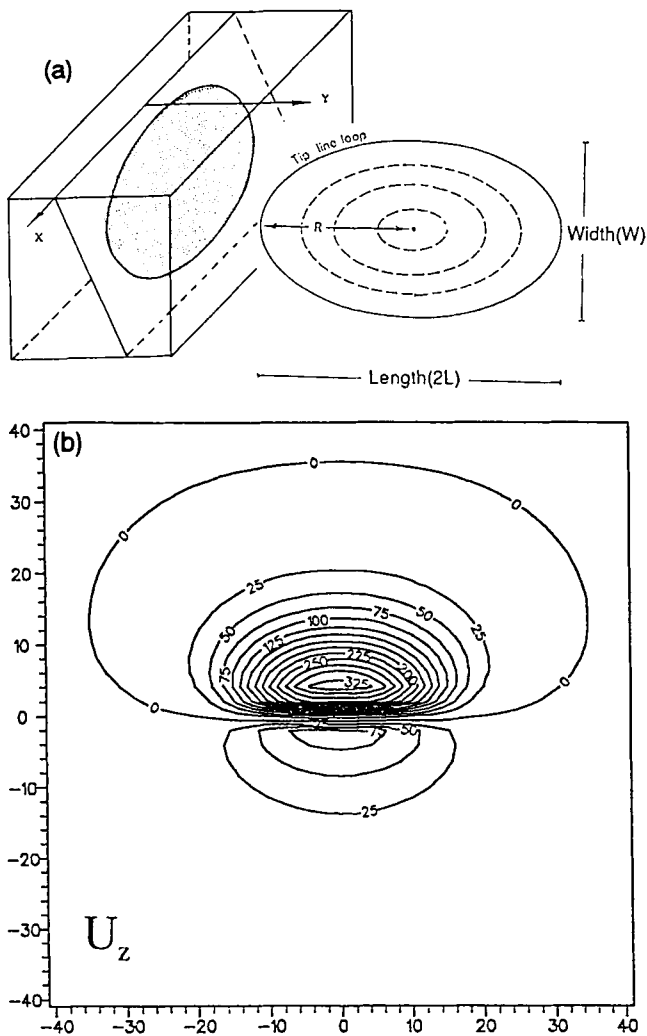
5 ELLIPTICAL FAULT WITH CUMULATIVE DISPLACEMENT

Field observations and seismic reflection data show that a fault surface, whether for a blind fault or one intersecting the free surface, is never rectangular, nor is the fault displacement constant. The fault geometry and displacements vary from fault to fault. Fault geometry and displacement information extracted from UK coal mine records and from high-resolution seismic reflection data from offshore UK has shown a systematic displacement variation for blind faults with fault dying out upwards, downwards and laterally (Barnett et al. 1987). An idealized blind fault has an elliptical fault surface defined by the zero displacement contour and displacement which varies from a point of maximum displacement at the centre to zero displacement at the tip-line. Contours of equal displacement form ellipses centred on the point of maximum displacement. The displacement gradient normally varies with direction on the fault surface, the ellipse usually being elongated laterally. Fig. 4(a) shows the displacement contour map for an idealized blind fault, and corresponds to those of the Watterson and Walsh fault growth model (Watterson 1986; Walsh & Watterson 1987). The fundamental concepts of the Walsh & Watterson (1987) fault growth model are that the slip increases linearly with fault radius as the fault grows so that the fault displacements increase approximately with the square of the fault width. For a fault growth model in which the maximum slip in successive slip events is increased by a constant amount, the cumulative displacement can be calculated. The formula (22) is an expression derived by Walsh & Watterson (1987) for the steady-state fault surface displacement profile for such a blind fault grown by multiple slip events.

$$d = 2\{[(1 + r)/2]^2 - r^2\}^{1/2}(1 - r), \tag{22}$$

where d is the normalized displacement at a point on a radius of the fault ellipse, and r is the normalized radial distance from the centre of the fault. The actual displacement at a point is obtained by multiplying the normalized displacement by the maximum displacement at the centre. The displacement distribution shown in Fig. 4(a) has been used to define the fault displacement distribution for our dislocation model throughout this section.

The computation procedures are similar to those for a rectangular fault. The displacement geometry differs in that the slip on the fault surface now varies from point to point, rather than having a constant value for a rectangular fault. Unit slip is assumed for all the point sources followed by linear scaling to incorporate displacement variation, since the $\mathbf{D}_m$ vector in (10) and (12) contains a factor $U_0 dS$ (with U_0 as the average dislocation on a point source and dS as the size of the rupture area) which can be factored out of any integrals in (17)–(19). After the integrals for point sources

Figure 4. (a) Cumulative displacement geometry on an elliptical fault of long axis 40 km and short axis 20 km. Note that the slip varies from maximum displacement (1 km) at the centre to zero displacement at the tip-line. (b) Vertical surface displacement (U_z) contour map for the 60° dip–slip fault intersecting the free surface. The observation horizon is the free surface. (c) Horizontal surface displacement (U_x) contour map. (d) Horizontal surface displacement (U_y) contour map.

Figure 4. (continued)

have been evaluated, the actual displacements due to an elliptical fault are obtained by multiplying the results from integrations by appropriate slips determined from (21).

Figs 4(b)–(d) show the vertical and horizontal surface displacement contour maps calculated for the elliptical fault growth model described above. The fault dips at 60° and intersects the free surface $(D = 0)$. It can be seen that the displacement values and deformed area in any one of the contour maps are smaller than those of the rectangular constant slip fault in Fig. 2. The concentric ellipse-like contours formed by equal horizontal displacement (U_x) in (c) are closer to each other than that for the rectangular fault. For the vertical displacement (U_z), the closed contours on both sides of the fault in Fig. 4(b) are less flattened than those in Fig. 2(b). The asymmetry of vertical displacements on both sides of the fault is still apparent.

Fault dip controls the displacement distribution and as a
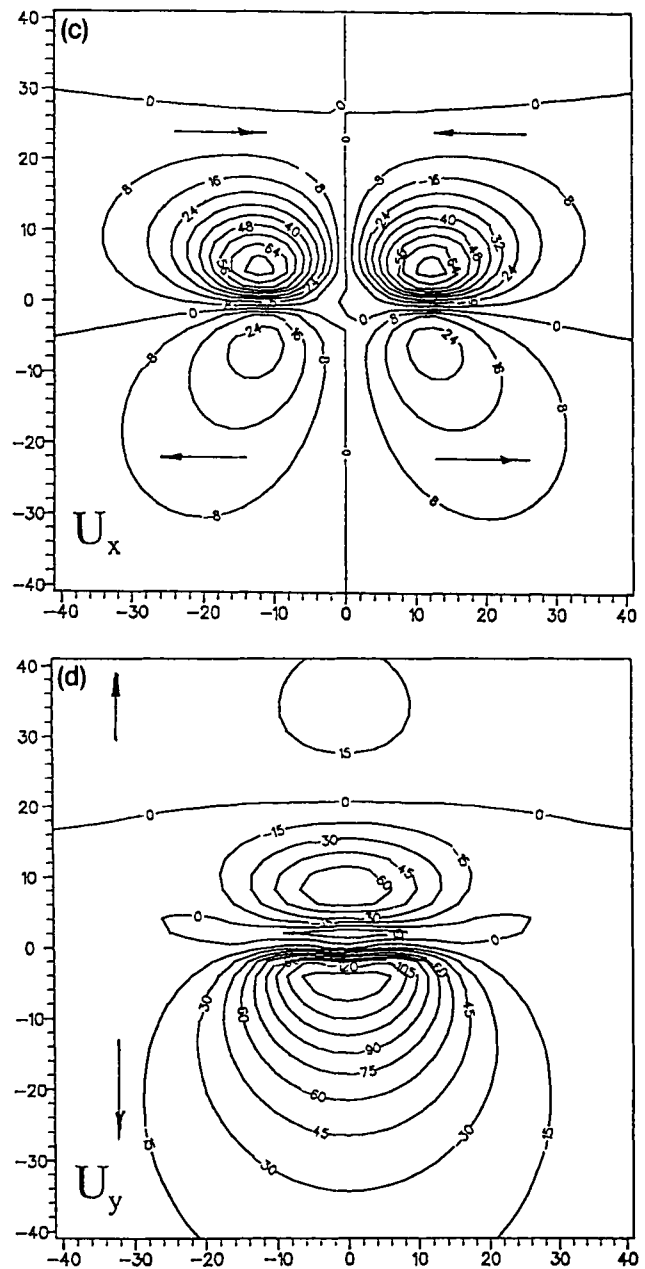
consequence the symmetry/asymmetry of displacement patterns on the downthrow and upthrow sides. It is well known that a vertical dip–slip fault displays an absolute symmetry in displacement on both sides. Any faults whose dips are less than 90° will show an asymmetry in vertical displacements, and the asymmetry increases with decreasing fault dips. The asymmetry is such that fault uplift is reduced relative to subsidence for a normal fault. At the same time, a decrease in fault dip is accompanied by a decrease in the vertical component of displacement. The ratios of the maximum amount of uplift to the maximum amount of subsidence on the free surface are about 1, 9, 24 and 100 per cent, corresponding to 30, 45, 60 and 90° dip–slip elliptical faults respectively. These ratios and their dependence on fault dip are different for the elliptical fault growth model and rectangular constant slip fault because of their different

displacement distributions [refer to fig. 3(a) of King, Stein & Rundle 1988—variation of the vertical surface displacement with dips for a rectangular fault of constant slip].

Subsurface fault displacement patterns differ profoundly from those of the surface. The displacement contour pattern is shown in Fig. 5 for a subsurface horizontal plane which intersects the centre of an elliptical blind fault. Fig. 5(a) is a perspective view of a blind fault and a subsurface horizon. The blind fault also dips at 60° and has a depth of 10 km below the free surface. Figs 5(b)–(d) show the three components of displacements U_z, U_x, U_y at a depth of 18.6 km, which corresponds to the depth of the horizontal plane cutting through the centre of the fault. The fault
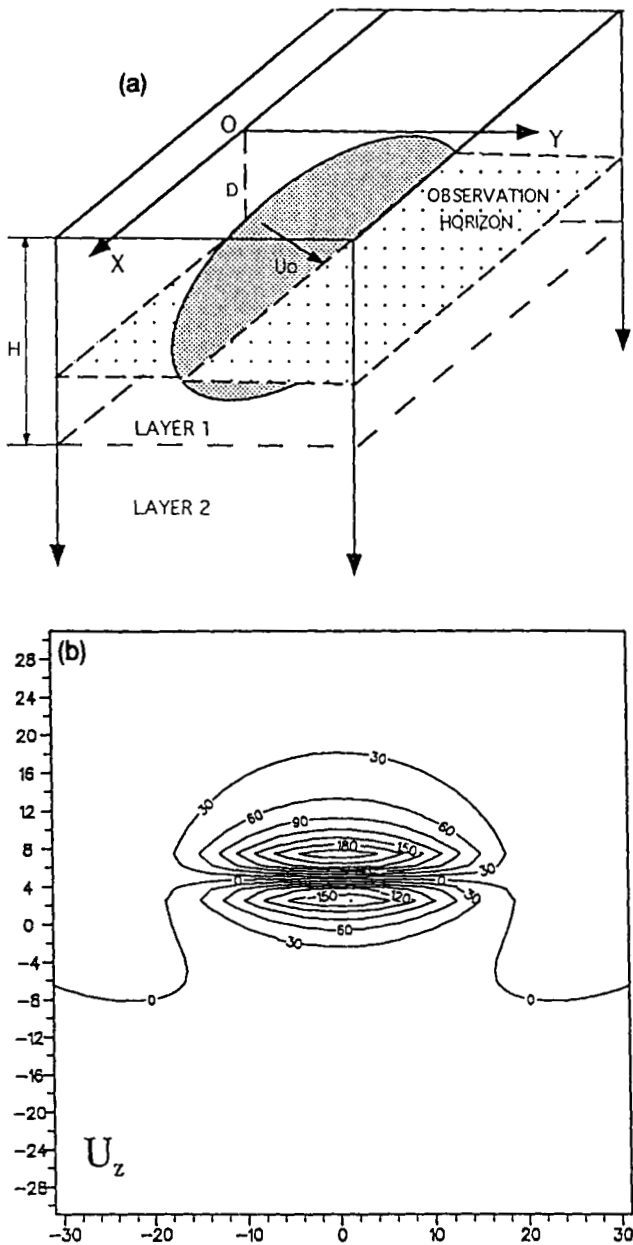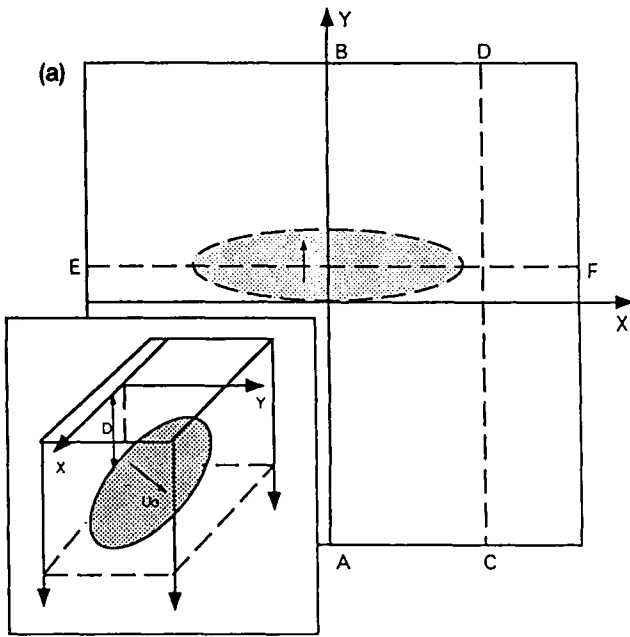

Figure 5. (a) Perspective view of an elliptical fault and an observation horizon. (b) Vertical displacement (U_z) contour map for a 60° dip–slip fault at depth $D = 10$ km. The observation horizon is originally horizontal and at depth $z = 18.6$ km, which cuts through the fault centre. (c) Horizontal displacement (U_x) contour map. (d) Horizontal displacement (U_y) contour map.
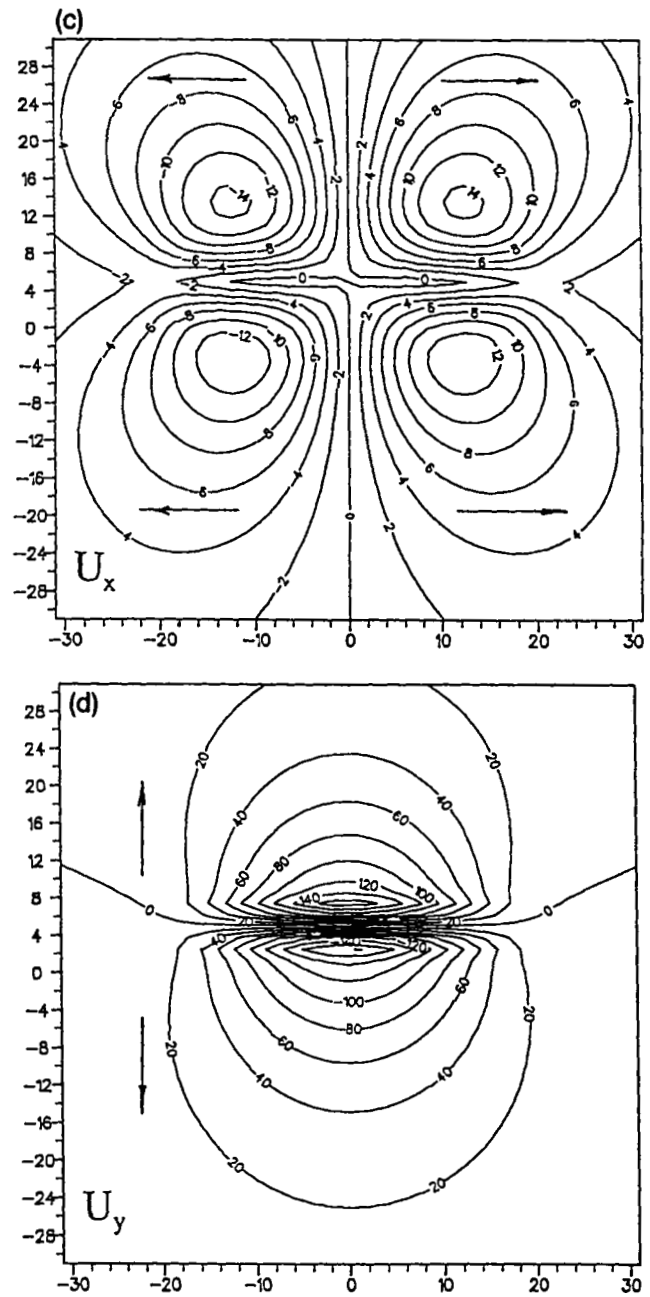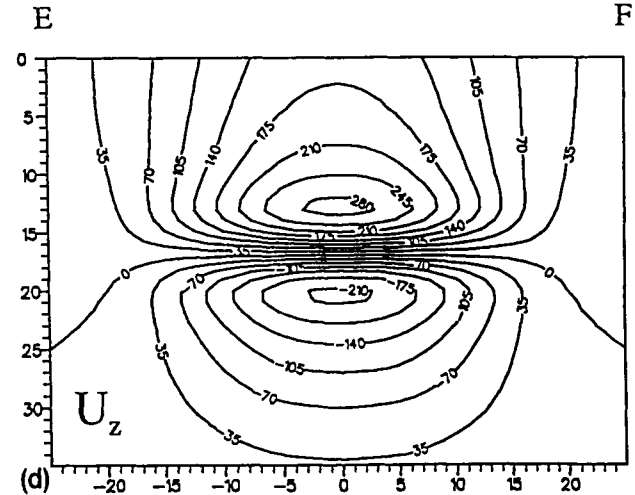
Figure 5. (continued)

displacement geometry is otherwise the same as in Fig. 4(a). Positive values in Fig. 5(b) correspond to subsidence while the negative values correspond to uplift. Note that although the horizon crosses the centre of the fault, the vertical displacement contour patterns are not symmetric on the downthrow and upthrow sides, i.e. there is a greater amount of subsidence than uplift. This is because the depth of the fault (10 km) is not great enough, compared to the dimension of the fault (width 20 km), to eliminate free-surface effects. A striking feature of the horizontal displacement (U_x) contour map of Fig. 5(c) is that, in contrast to the similar map in Fig. 2(c) for the rectangular fault, Fig. 5(c) shows outwards movement in a direction parallel to the strike of the fault on both sides of the fault.
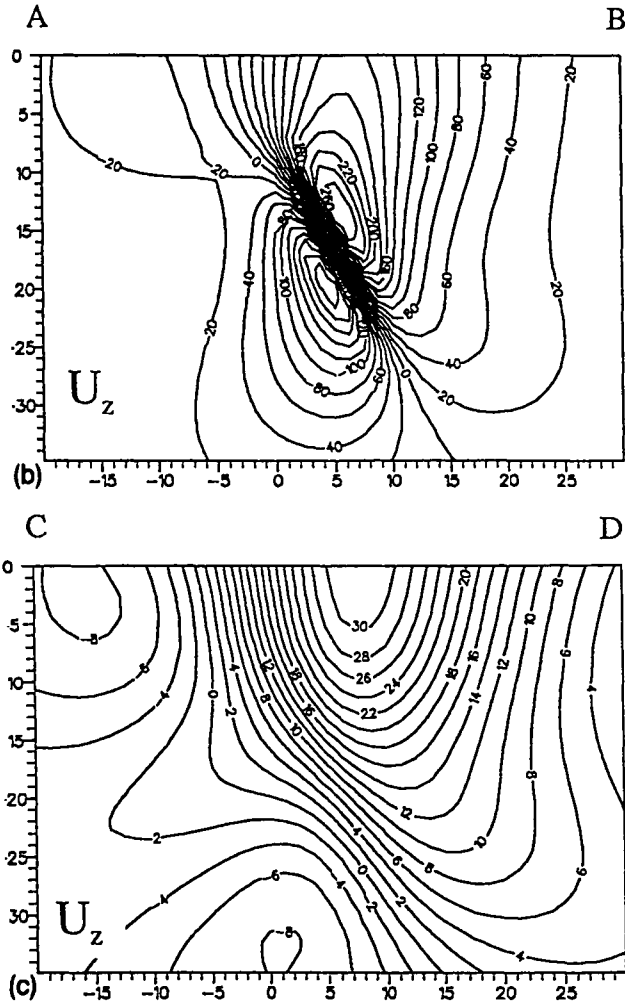
Figure 6. (continued)

The displacement contour patterns for U_y are almost symmetric with respect to the fault plane.

Vertical sections of the vertical displacement for the buried elliptical fault growth model are shown in Fig. 6. The locations of the vertical profiles are shown in Fig. 6(a). The general characteristics of contour patterns for profiles AB and EF are similar for the elliptical fault growth and rectangular fault models except for the reduced displacement values of the elliptical fault growth model. The two points of maximum displacements on both side of the fault in (b) are closer for the elliptical fault growth model than those for the rectangular fault. A conspicuous fault zone for profile CD which passes by the side of the elliptical fault is no longer evident. This is because the more realistic displacement distribution on the elliptical fault decreases strains near the edge of the fault.

6 STRAIN CHANGES ASSOCIATED WITH FAULTING

Strains can be used to characterize the extensions (contractions) and shear distortions of a material element in three dimensions. The generalized strain tensor usually has nine components which completely characterize the local state of strain. The strain tensor may be reduced to six independent parameters. The components of infinitesimal strain can easily be expressed in terms of displacement components:

$$\varepsilon_{xx} = \frac{\partial U_x}{\partial x}, \qquad \varepsilon_{xy} = \frac{\partial U_y}{\partial x} + \frac{\partial U_x}{\partial y},$$

$$\varepsilon_{yy} = \frac{\partial U_y}{\partial y}, \qquad \varepsilon_{yz} = \frac{\partial U_z}{\partial y} + \frac{\partial U_y}{\partial z}, \tag{23}$$

$$\varepsilon_{zz} = \frac{\partial U_z}{\partial z}, \qquad \varepsilon_{zx} = \frac{\partial U_x}{\partial z} + \frac{\partial U_z}{\partial x},$$

where U_x, U_y and U_z are the x, y and z components of displacement respectively. The quantities ε_{xx}, ε_{yy} and ε_{zz} are normal components of the strain tensor and ε_{xy}, ε_{yz}, ε_{zx} are shear components. The normal components of strain ε_{xx}, ε_{yy} and ε_{zz} are assumed, by convention, to be negative for compression and positive for tension. Volumetric strain

Figure 6. (a) Plan view of an elliptical fault and three vertical sections. The fault is at depth $D = 8$ km. (b) Vertical displacement contour map along the section AB from an elliptical fault with cumulative displacement. (c) Vertical displacement contour map along the section CD. (d) Vertical displacement contour map along the section EF.

may be defined as

$$\Delta = \varepsilon_{xx} + \varepsilon_{yy} + \varepsilon_{zz}. \qquad (24)$$

It is negative when the volume of the element is decreased by compression.

The 3-D subsurface displacement field for an elliptical fault growth model has been used to determine strain changes. The fault is at depth $D = 10$ km, and its displacement geometry is taken the same as in Fig. 4(a). Strain changes associated with faulting were calculated by finite difference using equation (23).
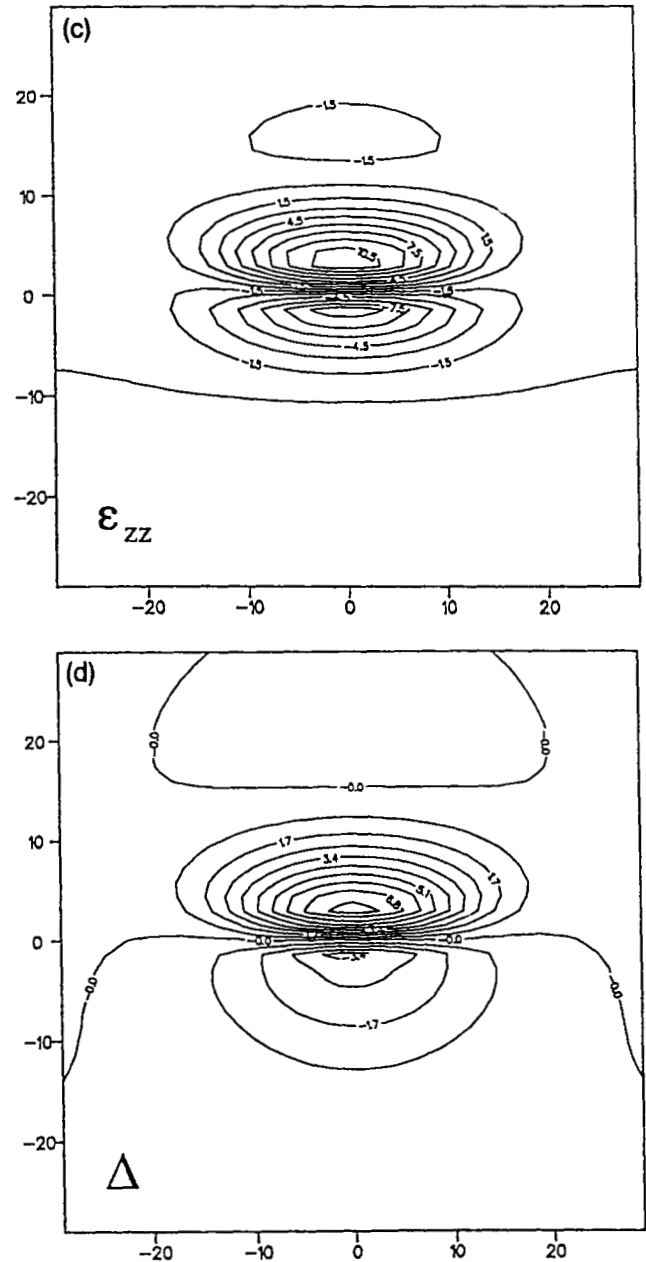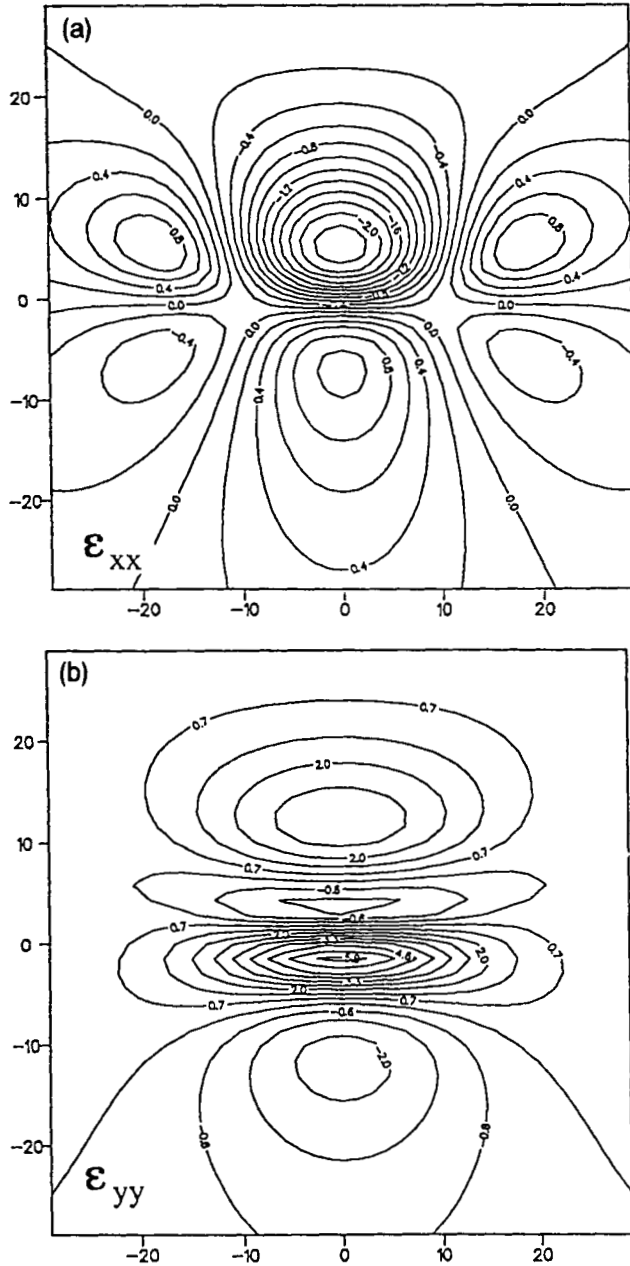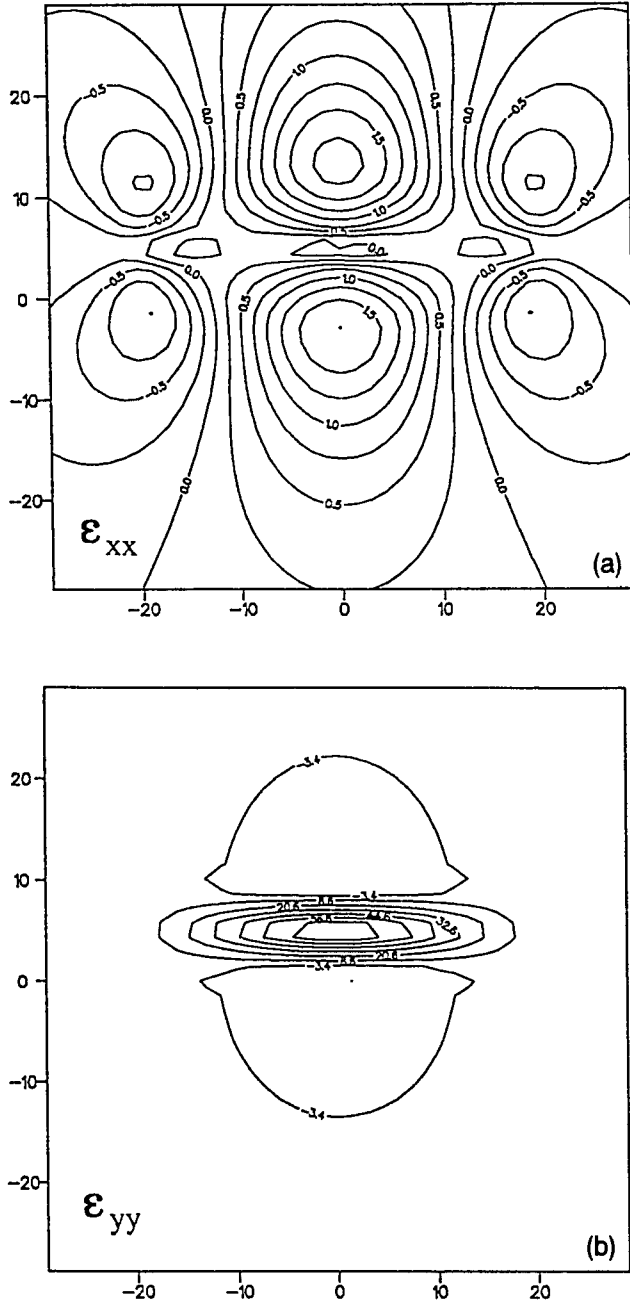

Figure 7. (a) Normal strain (ε_{xx}) contour map due to the fault defined in Fig. 4(a). The observation horizon is at depth $z = 8$ km, which is 2 km above the fault. The original strain values are multiplied by a scaling factor 1.0×10^3. Negative strain values correspond to contraction while positive values correspond to extension. (b) Normal strain (ε_{yy}) contour map. (c) Normal strain (ε_{zz}) contour map. (d) Volumetric strain (Δ) contour map.
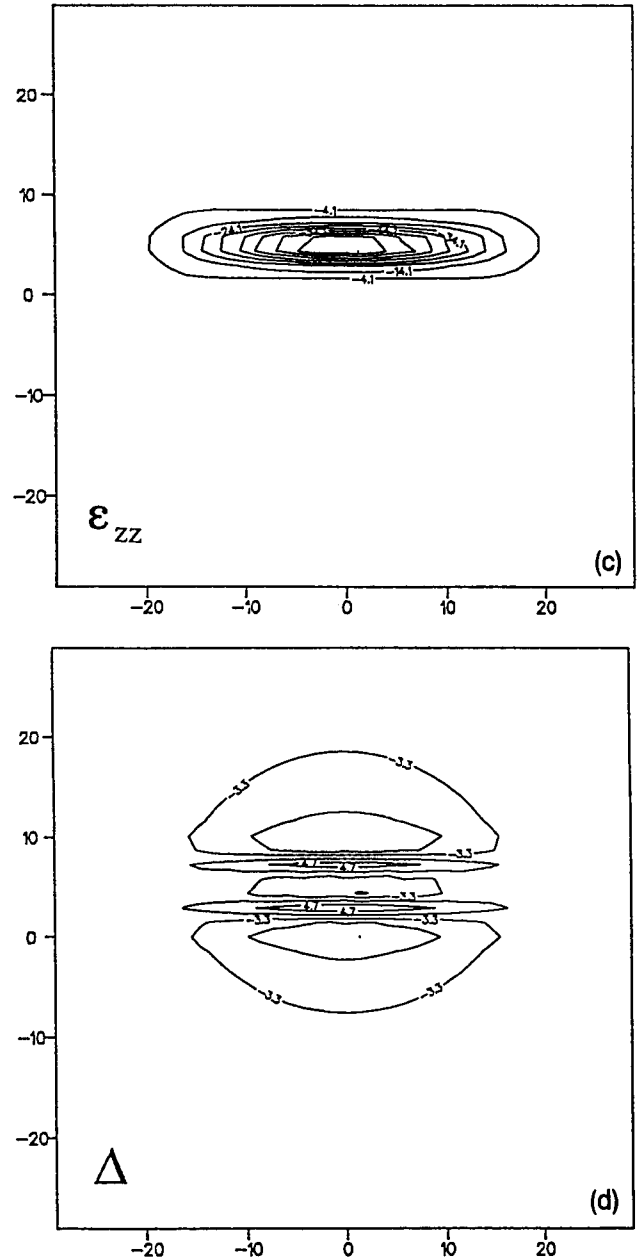

Figure 7. (continued)

Fig. 7 shows three normal strains and a volumetric strain on an initially horizontal plane $z = 8$ km. It can be seen that large strains are concentrated on the sides and faces of the elliptical fault and take the form of a pattern of positive and negative lobes (Fig. 7a). Fig. 7(a) also shows the contraction of material on the downthrow side indicated by negative strain values, and extension of material on the upthrow side by positive strain values. Fig. 7(b) shows large tensile ε_{yy} strains at the centre and compressive strains on the upthrow side. Fig. 7(c) shows the ε_{zz} strain distribution. The strain values for ε_{zz} are generally larger than the previous two components. It can be seen that large compressive ε_{zz} strain occurs on the upthrow side while extension occurs on the downthrow side of the fault. Fig. 7(d) shows the volumetric strain distribution. The contour pattern resembles that of Fig. 8(c), indicating that the 60° dip–slip normal faulting is dominated by vertical deformation, and that after faulting

there is an increase in volume on the downthrow side and a decrease in volume on the upthrow side.

When the observation horizon is through the fault centre, the strain field changes dramatically. Fig. 8(a) shows the ε_{xx} strain component. Here the signs of the strain values are the same on both sides of the fault, both indicating extensional deformation, whereas compression occurs at fault edges. Fig. 8(b) shows tensile strains (ε_{yy}) at the centre sandwiched by compressive strains on both sides. Fig. 8(c) demonstrates the domination of compressive ε_{zz} strains on this horizon. Note that the strain values in this figure are much larger

Figure 8. (a) Normal strain (ε_{xx}) contour map due to the fault defined in Fig. 4(a). The observation horizon is at depth $z = 18.6$ km, which is through the centre of the fault. The original strain values are multiplied by a scaling factor 1.0×10^3. (b) Normal strain (ε_{yy}) contour map. (c) Normal strain (ε_{zz}) contour map. (d) Volumetric strain (Δ) contour map.


Figure 8. (continued)

than in Fig. 7 corresponding to the greater deformation occurring on this level. The volumetric strain contour map in Fig. 8(d) indicates that there is an increase in volume in the area adjacent to the fault centre on the upthrow side, and a decrease in volume further away from the fault centre.

7 SINGLE SLIP EVENT FAULT

Slip refers to the fault displacement increment occurring during a single seismic event or cycle. Walsh & Watterson (1987) suggest that the maximum slip increases linearly with fault radius whereas maximum total displacement increases approximately with the square of the fault radius. The pattern of normalized displacement versus normalized distance from the centre of the fault is therefore different for the total displacement and individual event slip. Fig. 9(a)

(a)

(c)

(b)

(d)
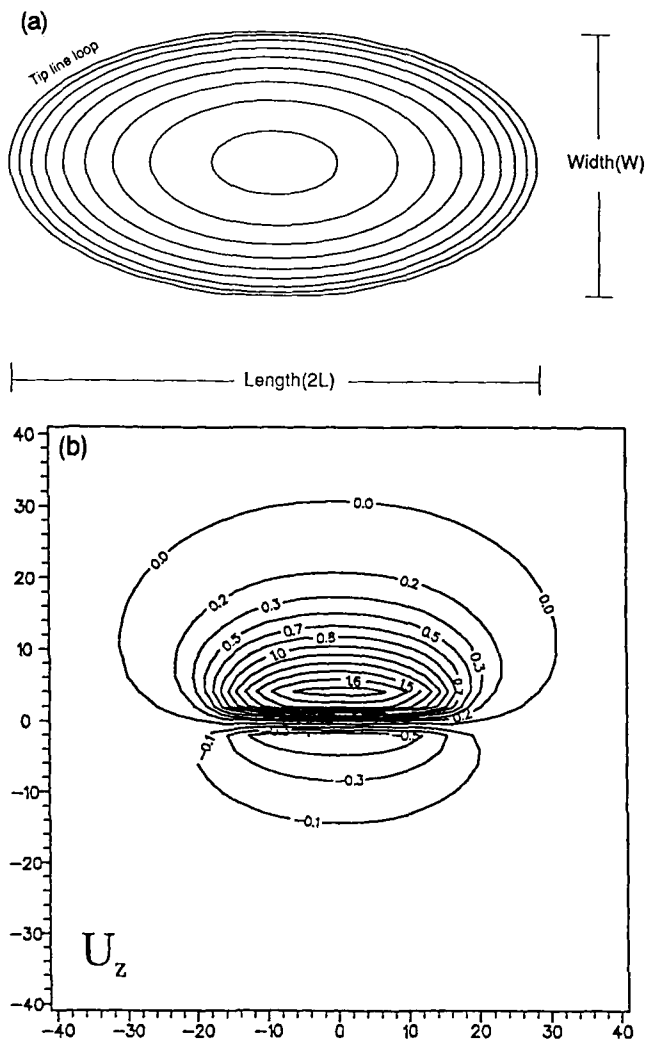
Figure 9. (a) Displacement geometry on a single slip event fault. The fault length $2L = 40$ km, and width $W = 20$ km. The maximum slip at the centre is 4 m. Note the displacement gradient near the tip-lines is higher than that near the central part of the fault. (b) Vertical displacement (U_z) contour map due to a single slip event fault dipping at $60°$. The fault intersects the free surface. The observation horizon is the free surface. (c) Horizontal displacement (U_x) contour map. (d) Horizontal displacement (U_y) contour map.

Figure 9. (continued)

shows the displacement distribution from a single slip event fault where the slip varies from a point of maximum slip (4 m) at the centre to zero slip at the tip-line. The slip contour pattern differs from that of the total displacement distribution shown in Fig. 4(a). Specifically, the slip gradient (change in displacement/radial distance) is higher within a narrow zone adjacent to the tip-line loop of the slip surface. For simplicity and comparison, we choose a fault with the same dimension as in Fig. 4(a). Let us suppose we have obtained by some means the slip profile of an active fault from the nth event as shown in Fig. 9(a). What is the displacement field caused by this single slip event fault, and how does it compare with that for the grown fault where the cumulative displacement distribution is used?

The vertical and horizontal displacement contour maps are shown at the surface for a single slip event in Figs
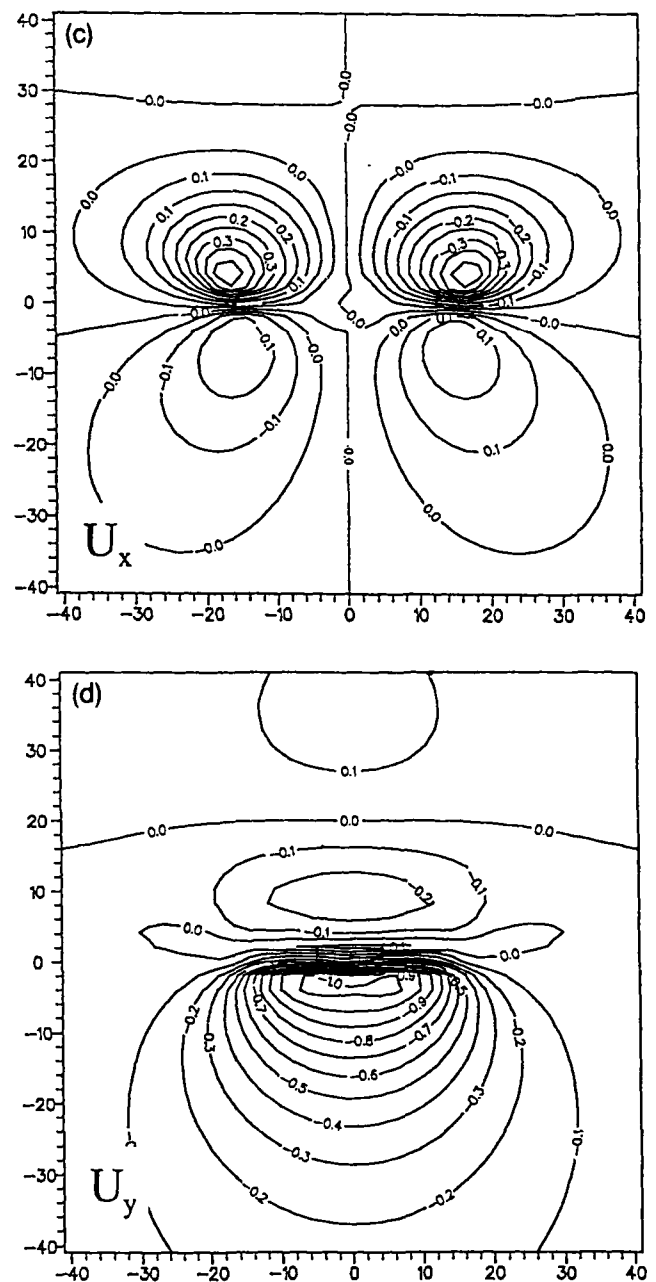
9(b)–(d). The fault dip is also taken as $60°$. The contour patterns resemble those of total displacement profile of the elliptical fault (see Fig. 4) but have sharper displacement gradient towards the edges.

8 OBLIQUE SLIP FAULT

So far, only dip–slip faults have been examined. The model can also be applied to a fault with oblique slip. Referring to Fig. 1(a), the rake β can be chosen as any values from 0 to $360°$. If $\beta = 0°$, the fault is strike–slip; if $\beta = 90°$, the fault is dip–slip; if $\beta = 270°$, the fault refers to a thrust fault. Mathematically, the displacements due to an oblique slip fault is a linear combination of displacements from a vertical strike–slip, a vertical dip–slip and a $45°$ dip–slip fault [see
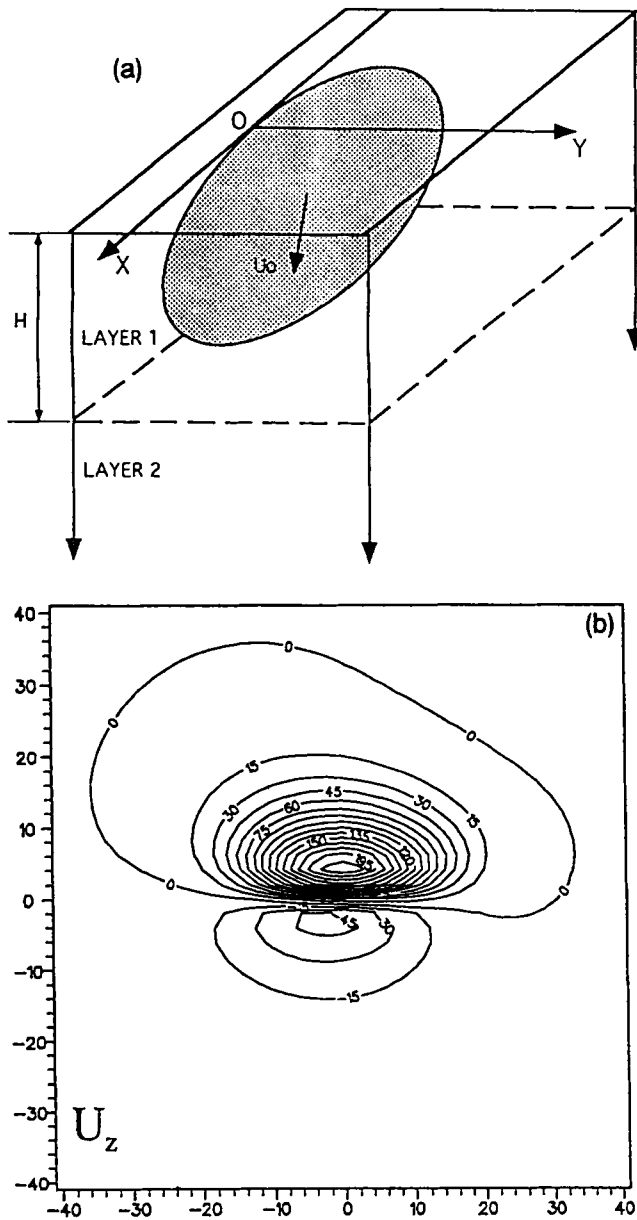
Figure 10. (a) An oblique slip fault dipping at 60°, and the rake (β) is 45°. The displacement geometry is the same as defined in Fig. 4(a). (b) Vertical displacement (U_z) contour map due to the oblique fault intersecting the free surface. The observation horizon is the free surface. (c) Horizontal displacement (U_x) contour map. (c) Horizontal displacement (U_y) contour map.

Figure 10. (continued)

formula (20)]. Figs 10(b)–(d) show the surface displacement patterns for an oblique slip fault intersecting the free surface. The fault has an elliptical shape and displacement gradient as predicted by Walsh & Watterson (1987). The fault parameters are the same as in Fig. 4 except for $\beta = 45°$. As would be expected there is a substantial difference in contour patterns compared to the pure dip–slip example especially for the two horizontal displacement components (see Figs 10c and d).

9 FAULT ARRAYS

It is rare to see a single isolated fault. Geological observation shows that the displacement fields of adjacent
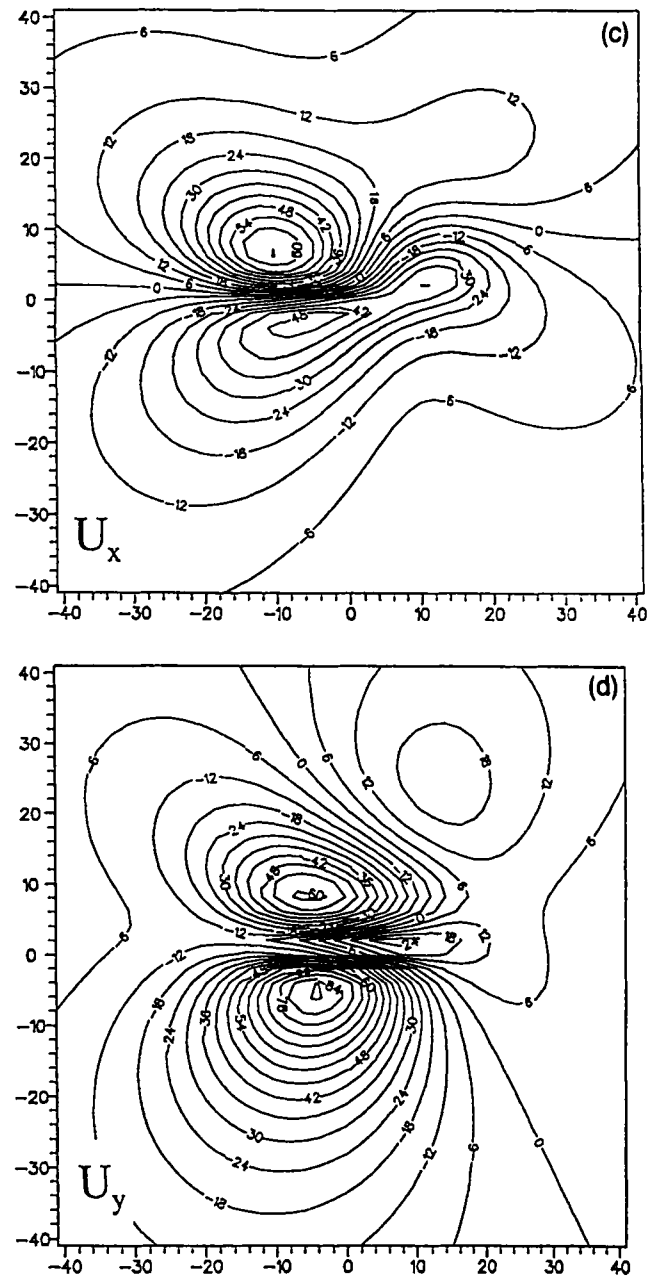
faults overlap, and that structure contours are resultants of displacements on multiple faults. To obtain the overall pattern of displacement contour maps for two or more faults, we must first consider the displacement field of isolated single faults separately; the composite displacement field may then be obtained by superposition of the displacement fields of individual faults. Fig. 11(a) is a plan view of two identical faults located 10 km apart. Both faults intersect the free surface. The fault parameters are the same as in the model of Fig. 4. Figs 11(b)–(d) show the overprinted displacement due to the fault array. The three contour plots clearly demonstrate how rocks deform within the fault overlap zone. Figs 12(b)–(d) show the vertical displacement contour maps on three vertical sections whose locations are given in Fig. 12(a). The vertical section of Fig. 12(b) shows two parallel faults and a highly deformed interference zone between them. For profile CD (Fig. 12c)
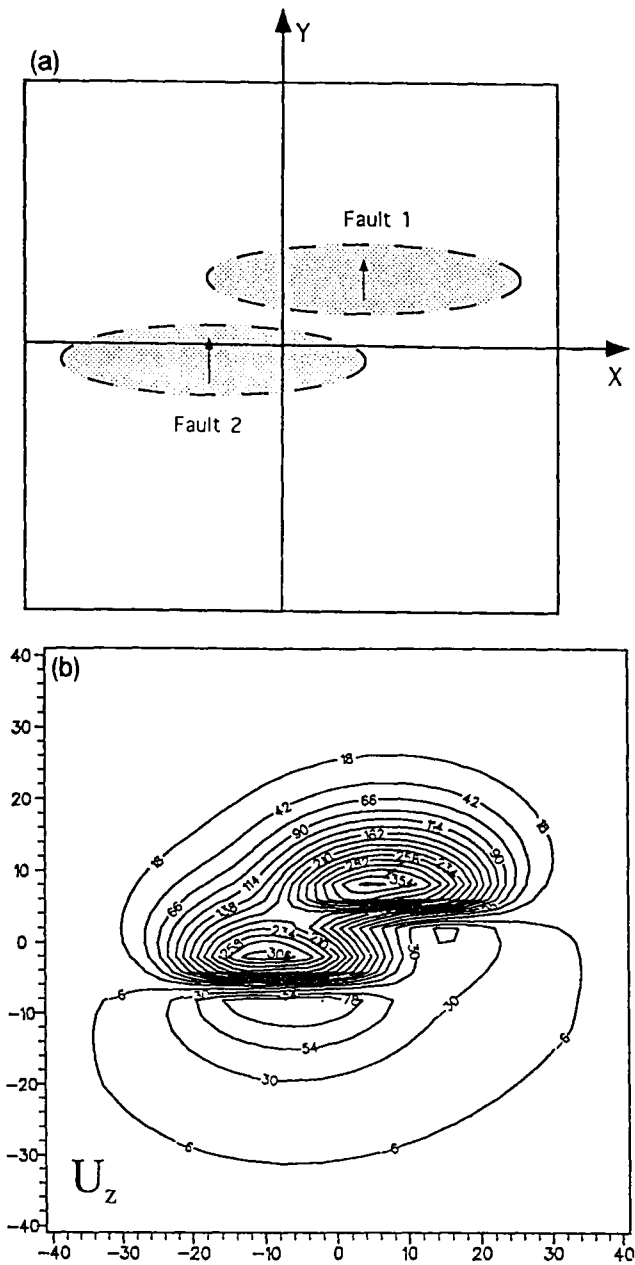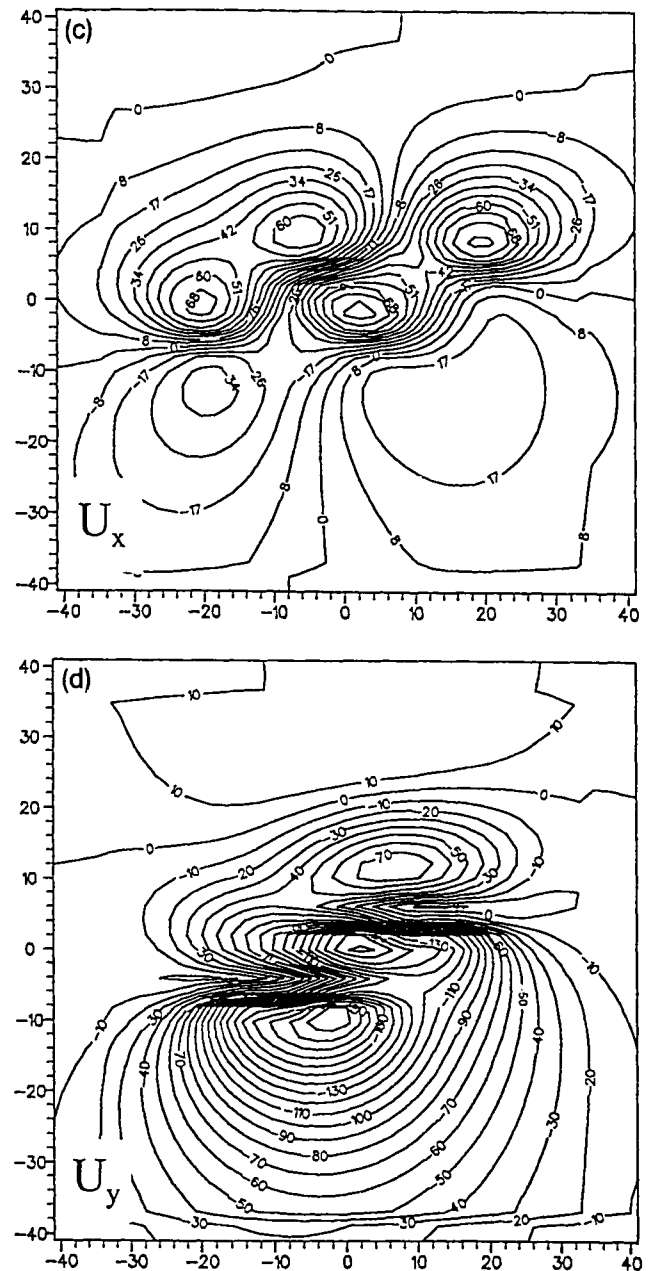
Figure 11. (a) Plan view of two identical faults intercepting the free surface ($D = 0$ km). Two faults dip towards the positive Y direction and are 10 km apart from each other. The observation horizon is the free surface. (b) Total vertical displacement field (U_z) due to the fault array. (c) Total horizontal displacement field (U_x). (d) Total horizontal displacement field (U_y).

Figure 11. (continued)

the two points of maximum displacements on both sides of the fault are shifted some distance towards the positive Y direction.

The theory described in this paper may be applied to fault systems of many faults of arbitrarily relative orientation and slip.
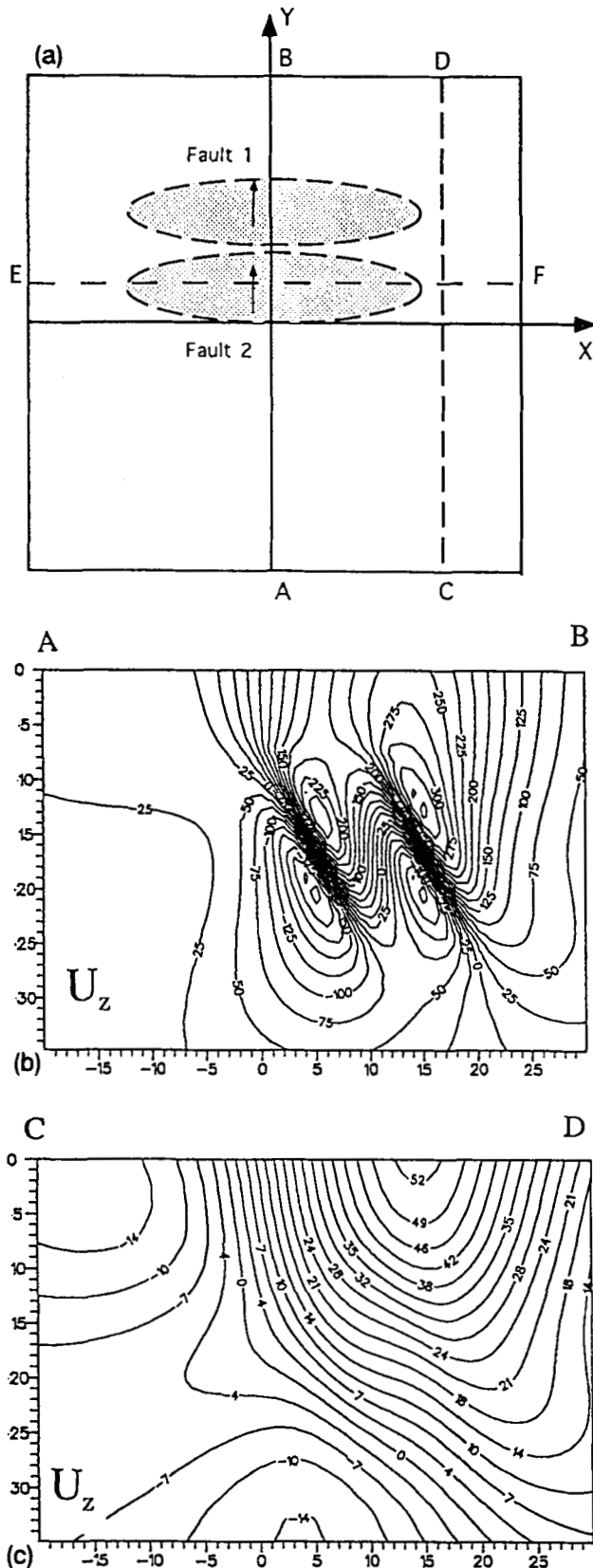
10   DISCUSSION

The elastic dislocation model described in this paper can only predict the coseismic deformation which occurs at the time of the earthquake. Although it does take into account fault growth, it does not consider the effects of gravity of fault-induced topography, of lower crustal plastic deformation, of lithosphere temperature and density field perturbations, or of erosion or sediment deposition. Other loads, whether positive or negative, will result in crustal deformation and regional-scale vertical displacement. The amount of vertical displacement will depend on the flexural rigidity of the lithosphere and the densities of crust and mantle (Kusznir, Marsden & Egan 1991). The isostatic loading effects on the final geological structure for a normal or a thrust fault cutting the free surface are greater than for a blind fault, because they generate greater surface culmination and subsidence than blind faults. The elastic dislocation model described in this paper does not take into account interseismic deformation due to the relaxation of
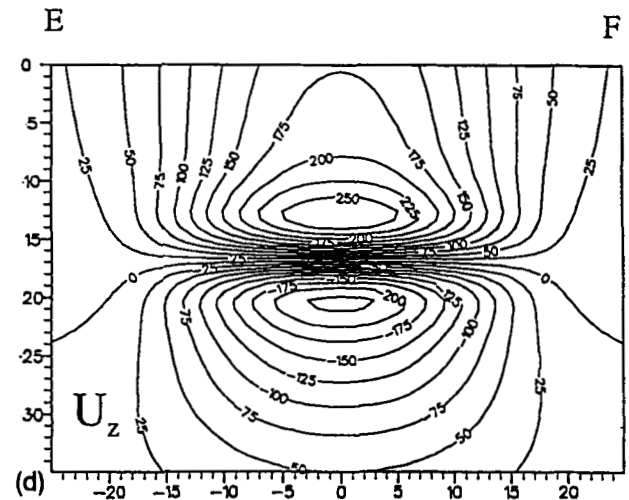
Figure 12. (continued)

stresses in the viscoelastic layer of the lower crust and mantle, nor its modification by isostasy, which play a large role in controlling the final crustal structure equilibrium.

So far, only planar faults have been considered. In practice, fault dips may vary with depth and with formation lithology. The variation of fault curvatures will affect the displacement geometry on the fault and control the displacement fields within a medium surroudning a fault. It is anticipated that future fault displacements models will be able to take into account viscoelastic and isostatic effects as well as variable fault curvature.

11 CONCLUSIONS

(1) Novel kernel functions for expressing displacements in the subsurface have been derived using the Thomson–Haskell Matrix technique. By combining the results of other workers with our newly derived expressions for subsurface displacement, it is possible to evaluate 3-D displacements at any points in the volume containing a fault.

(2) For the purpose of comparison with the existing model, a rectangular fault with constant slip has been modelled. The horizontal and vertical displacement fields have been computed for both surface and subsurface. The results for surface displacements are consistent with those determined by Rundle (1982).

(3) Surface and subsurface 3-D displacements have been calculated for an elliptical fault with cumulative growth displacements. The effects of fault dip and observation horizon depth on displacements have been explored. Displacements on various vertical sections within an elastic continuum have been computed using elastic dislocation theory.

(4) Surface and subsurface 3-D displacement may be determined not only for dip–slip faults but also for strike–slip and oblique slip faults.

(5) If the slip distribution on a single slip event fault is known, the surface and subsurface displacements associated with the fault may also be determined. As a consequence, the deformation associated with earthquake faulting may be used to derive earthquake parameters.

(6) The composite displacement field for a multiple fault

Figure 12. (a) Plan view of two identical faults and three vertical sections. The faults are at depth $D = 8$ km. (b) Vertical displacement contour map on the section AB. (c) Vertical displacement contour map on the section CD. (c) Vertical displacement contour map on the section EF.

array may be determined by superposing the displacement of individual isolated faults. This may be applied for faults of arbitrary relative orientation and slip.

(7) The three normal strain and volumetric strain changes in the subsurface volume containing a single fault have been determined and allow us to examine the distribution of extension and compression of material as a result of faulting. Cycling of volumetric strain may have implications for fluid flow.

(8) This subsurface dislocation model may be used to predict the subsurface displacement field from observed fault plane displacement distributions obtained for real faults using 3-D seismic reflection data.

ACKNOWLEDGMENTS

REFERENCES

Barnett, J., Mortimer, J., Rippon, J. H., Walsh, J. J. & Watterson, J., 1987. Displacement geometry in the volume containing a single normal fault, *Am. Ass. Petrol. Geol. Bull.*, **71**, 925–937.

Ben-Menahem, A. & Singh, S. J., 1968. Multipolar elastic fields in a layered half-space, *Bull. seism. Soc. Am.*, **58**, 1519–1572.

Ben-Manahen, A. & Gillon, A., 1970. Crustal deformation by earthquakes and explosions, *Bull. seism. Soc. Am.*, **60**, 193–215.

Chinnery, M. A., 1961. The deformation of the earth around surface faults, *Bull. seism. Soc. Am.*, **51**, 355–372.

Erdelyi, A., 1954. *Tables of Integral Transforms*, vol. II, McGraw-Hill Book Co., Inc.

Jovanovich, D. B., Husseini, M. I. & Chinnery, M. A., 1974a. Elastic dislocations in a layered half-space—I. Basic theory and numerical methods, *Geophys. J. R. astr. Soc.*, **39**, 205–217.

Jovanovich, D. B., Husseini, M. I. & Chinnery, M. A., 1974b.

Elastic dislocations in a layered half-space—II. The point source, *Geophys. J. R. astr. Soc.*, **39**, 219–239.

King, G. C. P., Stein, R. S. & Rundle, J. B., 1988. The growth of geological structures by repeated earthquakes, 1. Conceptual framework, *J. geophys. Res.*, **93**, 13 307–13 318.

Kusznir, N. J., Marsen, G. & Egan, S. S., 1991. A flexural–cantilever simple-shear/pure-shear model of continental lithosphere extension: Applications to the Jeanne d'Arc Basin, Grand banks and Viking Graben North Sea, in *The Geometry of Normal Faults*, Geological Society Special Publication No. 56, pp. 41–60, eds Roberts, A. M., Yielding, G. & Freeman, B.

Mansinha, L. & Smylie, D. E., 1971. The displacement fields of inclined faults, *Bull. seism. Soc. Am.*, **61**, 1433–1440.

Maruyama, T., 1964. Statical elastic dislocations in an infinite and semi-infinite medium, *Bull. Earthq. Res. Inst.*, **42**, 289–368.

Mikumo, T., 1973. Faulting process of the San Fernando earthquake of February 9, 1971 inferred from static and dynamic near field displacements, *Bull. seism. Soc. Am.*, **63**, 249–269.

Roth, F., 1990. Subsurface deformations in a layered elastic half-space, *Geophys. J. Int.*, **103**, 147–155.

Rundle, J. B., 1982. Viscoelastic-gravitational deformation by a rectangular thrust fault in a layered earth, *J. geophys. Res.*, **87**, 7787–7796.

Rybicki, K., 1971. The elastic residual field of a very long strike–slip fault in the presence of a discontinuity, *Bull. seism. Soc. Am.*, **61**, 79–92.

Sato, R., 1971. Crustal deformation due to dislocation in a multilayered medium, *J. Phys. Earth*, **19**, 29–46.

Savage, J. G. & Hastie, L. M., 1966. Surface deformation associated with dip–slip faulting, *J. geophys. Res.*, **71**, 4897–4904.

Singh, S. J., 1970. Static deformation of a multilayered half-space by internal sources, *J. geophys. Res.*, **75**, 3257–3262.

Steketee, J. A., 1958a. On Volterra's dislocations in a semi-infinite elastic medium, *Can. J. Phys.*, **36**, 192–205.

Steketee, J. A., 1958b. Some geophysical applications of the elasticity theory of dislocations, *Can. J. Phys.*, **36**, 1168–1198.

Watterson, J., 1986. Fault dimensions, displacements and growth, *Pure appl. Geophys.*, **124**, 355–373.

Walsh, J. J. & Watterson, J., 1987. Distributions of cumulative displacement and seismic slip on a single normal fault surface, *J. Struct. Geol.*, **9**, 1039–1046.